

Invited Review Paper

Modeling and Simulation of a Turbulent-like Thermal Plasma Jet for Nanopowder Production

Masaya Shigeta^a, Non-member

This paper discusses theoretical models and numerical methods to simulate turbulent thermal plasma flow transporting a nanopowder. In addition to a thermal plasma flow model, a sophisticated model is described mathematically for the nanopowder's collective growth by homogeneous nucleation, heterogeneous condensation, and coagulation among nanoparticles, and also transport by convection, diffusion, and thermophoresis, simultaneously. Demonstrative simulations show clearly that a suitable numerical method with high-order accuracy should be used for long and robust simulation capturing multiscale eddies and steep gradients of temperature, which are the turbulent features of thermal plasma flows with locally variable density, transport properties and Mach numbers. Eddies are first generated at the interfacial region between the plasma jet and ambient nonionized gas by fluid-dynamic instability. As a result of the eddies' generation–breakup process, the plasma flow entrains the ambient cold gas and deforms its shape traveling downstream. Numerous sub-nanometer particles are generated by nucleation and condensation in the thin layers near the plasma jet. Those particles diffuse and increase their size, thus decreasing their number by coagulation. Cross-correlation analysis suggests that the nanopowder distribution distant from a plasma jet can be controlled by controlling the temperature fluctuation at the upstream plasma fringe. © 2018 Institute of Electrical Engineers of Japan. Published by John Wiley & Sons, Inc.

Keywords: thermal plasma; fluid dynamic instability; turbulence; nanopowder; modeling

Received 2 June 2018; Revised 29 September 2018

1. Introduction

1.1. Thermal plasma for nanopowder production

A plasma is generated by a high-power discharge at around atmospheric pressure. Since its state is mostly in local thermodynamic equilibrium (LTE), it is called a 'thermal plasma'. It offers a unique flow with high temperatures of not only electrons but also heavy species, high chemical reactivity, intense light emission, and variable properties [1]. Because the plasma is also an electrically conductive fluid, it responds to an electromagnetic field. Therefore, its plasma state can be sustained by Joule heating and controlled by Lorentz force [2–6]. The thermal plasma has been used as a powerful tool for a variety of industrial applications [7]: e.g. plasma spray processes [8], waste treatment [9], arc welding [10], plasma cutting [11], and nanopowder production [12].

In particular, nanopowders have attracted much attention because they exhibit unique electronic, optical, and catalytic properties, which differ from those of larger particles of micrometer size or bulk materials [13]. Therefore, nanopowders, which comprise numerous nanometer-sized particles (nanoparticles), have been in increasing demand for various applications such as industrial, biomedical, and environmental purification processes. However, the practical mass production of high-quality nanopowders using conventional ways is still difficult, involving syntheses from liquid phases or requiring combustion. To overcome this shortcoming, the thermal plasma has been considered as a promising technique for the efficient fabrication of nanopowders [12]. A thermal plasma with very high temperature of approximately 10 000 K can vaporize even materials having a high melting or boiling point [14–18]. Furthermore, a thermal plasma has a steeply decreasing temperature gradient at its fringe, where the material vapor rapidly

changes into nanopowder. Taking advantage of these two characteristics, thermal plasma has achieved the one-step production of nanopowders with very high yields [19–21].

However, the precise control of the process is still difficult because the nanopowder growth and transport must be controlled simultaneously. A process involving collective growth by nucleation, condensation, and coagulation, and transport by convection, diffusion, and thermophoresis in or around a plasma is a remarkably intricate mass transfer problem in the microsecond to millisecond time scales. At present, it seems impossible for experiments to allow direct observation or measurement of such a spatial and temporal multiscale process. For this reason, the detailed mechanism remains unknown. The process design entails high expenditures of time and funds, depending on the engineers' experience.

Theoretical and computational approaches can clarify that mechanism. Particularly, models based on aerosol dynamics have been used to study nanopowder production using several types of thermal plasmas, as described in an earlier review article [12]. By virtue of the efforts of several groups, the spatial distributions of nanopowder around plasmas or in downstream chambers have been clarified while taking account of both growth and transport under various conditions [22–33]. However, all those simulations were restricted in the steady fields of the nanopowder as well as the plasma flow. In fact, as revealed in an earlier report [34], thermal plasma flows interacting with ambient nonionized cold gas are not steady but very dynamic, as are most fluid flows in nature. The author believes that such a dynamic thermal flow field is one cause of the widely dispersed size distributions in nanopowders produced by thermal plasmas. Therefore, it is important to investigate the simultaneous growth and transport of nanopowder in a dynamic thermal flow field. Moreover, it is necessary to clarify the correlation between the dynamic behavior of a plasma flow and the transient formation of nanopowder distribution, which has not been addressed by steady-state simulations or experiments to date.

^a Correspondence to: Masaya Shigeta. E-mail: shigeta@jwri.osaka-u.ac.jp

Joining and Welding Research Institute, Osaka University, 11-1, Mihogaoka, Ibaraki-shi Osaka, 567-0047, Japan

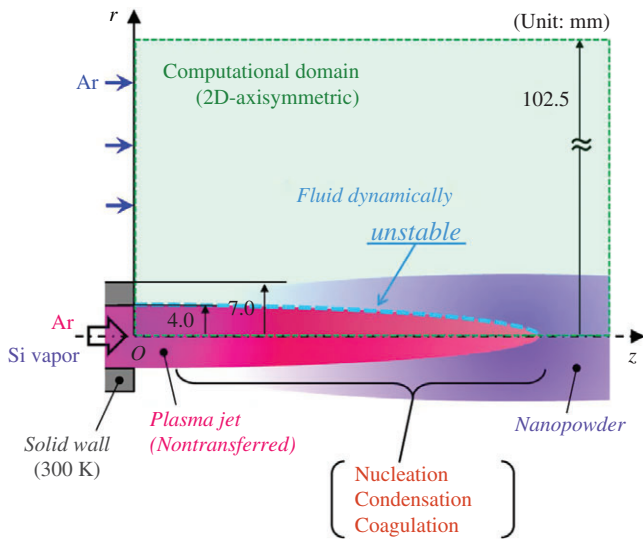


Fig. 1. Schematic illustration of a thermal plasma jet for nanopowder production

1.2. Turbulence of thermal plasma flows Turbulence of thermal plasma flows has been recognized as an important matter because it affects the process qualities of applications. Turbulence offers strong mixing effects on the momentum, energy, and material molecules and particles because of its eddies. For nanopowder production, the nanoparticles are generated not in the high-temperature plasma core but in the interfacial regions between the plasma and the cold gas at low to intermediate temperatures. Lower temperature regions tend to be more turbulent with multiscale eddies as discussed on the basis of Kolmogorov's theory in the literature [35]. These eddies strongly affect the transport processes of nanoparticles.

Pfender *et al.* [34] investigated the turbulence structures of direct current (DC) thermal plasma jets using Schlieren photography and conditional sampling techniques. They experimentally revealed that the low-temperature regions have complex structures with multiscale eddies, whereas the high-temperature regions appeared to be less turbulent. Hlína and colleagues [36–39] investigated the dynamic behaviors of the core of a thermal plasma jet by optical measurements and image-processing techniques. However, in spite of those works with great efforts, the turbulence characteristics of thermal plasma jets still remain unknown.

Why do thermal plasmas have turbulent (or at least turbulent-like) flow fields? Let us think about a thermal plasma jet, one of the simplest thermal plasma flows, which is a high-temperature, high-speed flow ejected from a nozzle (see Fig. 1). Pfender *et al.* [34] proved that a thermal plasma jet forms eddies, entraining ambient cold gas at its fringe. These eddies break into smaller eddies. Eventually, the plasma jet transitions into a turbulent state with multiscale eddies. This fact seems natural because a fluid jet is too unstable to keep itself laminar. Reportedly, a circular jet has a very low critical Reynolds number of 10.5–11.8 [40]. The fundamental cause of this turbulence transition process is the inherent fluid-dynamic instability at the jet fringe with a strong velocity shear, which grows and then rolls the fringe up to the eddies. At the discharge stages, a thermal plasma already has a spatially and temporally nonuniform profile because of unstable arc restrikes [41,42] sometimes with multiple roots [43] in a DC torch. However, these factors are merely additional disturbances promoting the turbulence transition. Excluding these additional factors, under sophisticated conditions, the fundamental mechanisms of turbulence transition of a thermal plasma affecting nanopowder should be clarified.

1.3. Purpose of this paper This paper discusses theoretical models and numerical methods to simulate especially a turbulent-like thermal plasma jet transporting nanopowder. In addition to the thermal plasma jet model, a sophisticated model is described mathematically for the nanopowder's collective growth by homogeneous nucleation, heterogeneous condensation, and coagulation among nanoparticles, and also transport by convection, diffusion, and thermophoresis simultaneously. Demonstrative simulations are performed to visualize a thermal plasma jet that is deformed by multiscale eddies as a result of its own fluid-dynamic instability and the consequent nanopowder distribution. The importance of numerical methods to express the dynamics is highlighted as well.

2. Model Description

2.1. Outline of the process and assumptions

Figure 1 shows a schematic illustration of nanopowder production using a nontransferred thermal plasma jet generated under atmospheric pressure. A plasma jet of argon gas is ejected from the nozzle. Assuming that the precursor material was already vaporized in the nozzle, silicon vapor is supplied with the plasma flow. Transported downstream by convection, the silicon vapor also diffuses toward the plasma's fringe, which is an interface between the high-temperature plasma and low-temperature nonionized gas. Therein, the vapor experiences a rapid temperature decrease and becomes highly supersaturated. That supersaturated state engenders homogeneous nucleation, which generates numerous nuclei. Once the nuclei are generated, the vapor condenses on the nuclei by heterogeneous condensation. Consequently, particles of nanometer size are created. These sequential processes constitute the fundamental growth processes of nanoparticles. Simultaneously, the nanoparticles mutually collide, coagulate, and merge. This coagulation also plays an important role in the collective growth of the particles. In addition, because the plasma fringe is fluid-dynamically unstable, the plasma jet naturally deforms and entrains ambient cold gas. It eventually transitions to turbulent flow with a complex temperature field [34]. In such a thermal flow field, the growing nanopowder is simultaneously transported by convection, diffusion, and thermophoresis.

This paper specifically pays attention to how the fluid-dynamic instability of a thermal plasma flow affects the nanopowder distribution. Therefore, other disturbing factors such as arc restriking in the nozzle or external injection of precursor materials into the plasma flow are excluded reasonably, although they have considerable influences in actual processes. Under this ideal condition, only the fluid-dynamic instability can deform a thermal plasma flow toward a turbulent state, following its growth especially at the plasma fringe with strong velocity shear. To capture this nature, the computation requires a fine mesh system and long time integration with a short interval, which entails considerably high computational costs. To reduce those costs, the models for the plasma flow and the nanopowder growth are formulated with several typical assumptions: (i) the whole fluid region including the plasma and the nonionized gas is in an LTE state; (ii) the plasma is optically thin; (iii) the fields are two-dimensional axisymmetric; (iv) the nanopowder consists of liquid spherical nanoparticles with a temperature identical to that of the fluid surrounding them; (v) the electric charge effects are neglected; and (vi) the material vapor is treated as an ideal gas.

The plasma jet actually forms a three-dimensional turbulent-like flow [34]. A three-dimensional simulation involves enormous computational time and costs. However, assumption (iii) of two-dimensional fields is validly adopted to highlight the elemental structures of the plasma field and nanopowder distribution that appear locally in an actual turbulent flow. Furthermore, this paper

especially focuses on nanopowder formation close to the plasma. The generated particles have diameters ranging from subnanometers to a few nanometers. Therefore, it can be taken as in assumption (iv), that is, they are still liquid because of the effect of melting point depression for very small particles [44]. This assumption supports the observation that, because of surface tension, the coagulated particles form not beads but a larger spherical particle.

2.2. Governing equations of thermal plasma flow

A thermal plasma is described effectively by a thermal fluid-dynamic approximation. The governing equations are the conservation equations of mass, momentum, and energy:

$$\frac{\partial \rho}{\partial t} + \nabla \cdot (\rho \mathbf{u}) = 0, \quad (1)$$

$$\frac{\partial}{\partial t}(\rho \mathbf{u}) + \nabla \cdot (\rho \mathbf{u} \mathbf{u}) + \nabla P - \nabla \cdot \left\{ \eta \left[2\mathbf{S} - \frac{2}{3}(\nabla \cdot \mathbf{u})\mathbf{I} \right] \right\} = 0, \quad (2)$$

and

$$\begin{aligned} \frac{\partial}{\partial t}(\rho h) + \nabla \cdot (\rho \mathbf{u} h) - \nabla \cdot \left(\frac{\lambda}{C_p} \nabla h \right) \\ - \frac{\partial P}{\partial t} - \mathbf{u} \cdot \nabla P + Q_{\text{rad}} - Q_{\text{con}} - \Phi = 0, \end{aligned} \quad (3)$$

where ρ stands for the density of the fluid, t represents the time, \mathbf{u} is the velocity vector, P denotes the pressure, η signifies the viscosity, \mathbf{I} is the unit matrix, h is the enthalpy, λ is the thermal conductivity, C_p is the specific heat at constant pressure, Q_{rad} represents the radiation loss, Q_{con} denotes the heat generation attributable to condensation, and Φ denotes the viscous dissipation. Furthermore, \mathbf{S} is the velocity strain tensor, defined as;

$$\mathbf{S} = \frac{1}{2}[(\nabla \mathbf{u}) + (\nabla \mathbf{u})^{\text{tr}}], \quad (4)$$

where the superscript tr denotes the transposition.

2.3. Governing equations of growth and transport of nanopowder

In engineering timescales and spatial scales, the aerosol dynamics approach effectively expresses the simultaneous processes of collective growth and transport of nanopowder around a thermal plasma. This section extends a previous model [45], which simply describes the birth and collective growth of nanopowder through homogeneous nucleation, heterogeneous condensation, and coagulation among the nanoparticles. First, those equations are derived briefly. The net production rate of the nanoparticles, which consist of g monomers, or g -mers, is written as

$$\frac{dn_p}{dt} = J - 2\sqrt{2}\beta_0 g^{1/6} n_p^2, \quad (5)$$

where n denotes the number density, with subscript p denoting ‘particle’. J is the homogeneous nucleation rate in the self-consistent nucleation theory modified by Girshick *et al.* [46] as

$$J = \frac{\beta_0 n_v n_s}{3} \sqrt{\frac{\Theta}{\pi}} \exp \left\{ \Theta - \frac{4\Theta^3}{27[\ln(n_v/n_s)]^2} \right\} \quad (6)$$

and

$$\Theta = \frac{\sigma s_v}{k_B T}. \quad (7)$$

In addition, β_0 is the parameter related to collision frequency, given as

$$\beta_0 = \left(\frac{3v_v}{4\pi} \right)^{1/6} \sqrt{\frac{6k_B T v_v}{m_v}} \quad (8)$$

for the free molecular regime. In these equations, σ represents the surface tension, s represents the surface area, v is the volume, m

is the mass, k_B is the Boltzmann’s constant, and T denotes the temperature. The subscripts v and s , respectively, denote ‘vapor’ and ‘saturation state’. In (5), the first and second terms express the increase rate by nucleation and the decrease rate by coagulation, respectively. Condensation does not change the particle number.

The total number of monomers composing all particles per unit volume increases through nucleation and condensation, although it does not change through coagulation. That increase in rate is written as

$$\frac{d}{dt}(n_p g) = J g_c + g^{2/3} \beta_0 (n_v - n_s) n_p, \quad (9)$$

where g_c denotes the number of monomers composing a particle in a critical state, given as

$$g_c = \left[\frac{2\Theta}{3 \ln(n_v/n_s)} \right]^3. \quad (10)$$

Here, introducing the new variable $f = n_p g$, (5) and (9) are rewritten as

$$\frac{dn_p}{dt} = J - 2\sqrt{2}\beta_0 n_p^{11/6} f^{1/6} \quad (11)$$

and

$$\frac{df}{dt} = J g_c + \beta_0 (n_v - n_s) n_p^{1/3} f^{2/3}. \quad (12)$$

The number of monomers conserved when the vapor changes its phase into particles is

$$\frac{dn_v}{dt} = -\frac{df}{dt}. \quad (13)$$

This simple set of equations (11)–(13) describes the simultaneous process by which particles are generated and grow collectively through homogeneous nucleation and heterogeneous condensation from a supersaturated vapor as well as mutual coagulation. This set gives the particle number density and the mean size, which agree almost perfectly with those obtained by the method of moment requiring much more complex formulations [45].

To obtain the spatial distribution of the nanopowder growing in a flow field, (11)–(13) are implemented into the convection–diffusion equations for n_p , f , and n_v as the source terms, as

$$\begin{aligned} \rho \frac{\partial}{\partial t} \left(\frac{n_p}{\rho} \right) + \rho \mathbf{u} \cdot \nabla \left(\frac{n_p}{\rho} \right) - \nabla \cdot \left[\rho D_p \nabla \left(\frac{n_p}{\rho} \right) \right] \\ - J + 2\sqrt{2}\beta_0 n_p^{11/6} f^{1/6} + \nabla \cdot \left(K_{\text{th}} \eta \frac{n_p}{\rho} \nabla \ln T \right) = 0, \end{aligned} \quad (14)$$

$$\begin{aligned} \rho \frac{\partial}{\partial t} \left(\frac{f}{\rho} \right) + \rho \mathbf{u} \cdot \nabla \left(\frac{f}{\rho} \right) - \nabla \cdot \left[\rho D_p \nabla \left(\frac{f}{\rho} \right) \right] \\ - J g_c - \beta_0 (n_v - n_s) n_p^{1/3} f^{2/3} + \nabla \cdot \left(K_{\text{th}} \eta \frac{f}{\rho} \nabla \ln T \right) = 0 \end{aligned} \quad (15)$$

and

$$\begin{aligned} \rho \frac{\partial}{\partial t} \left(\frac{n_v}{\rho} \right) + \rho \mathbf{u} \cdot \nabla \left(\frac{n_v}{\rho} \right) - \nabla \cdot \left[\rho D_v \nabla \left(\frac{n_v}{\rho} \right) \right] \\ + J g_c + \beta_0 (n_v - n_s) n_p^{1/3} f^{2/3} = 0 \end{aligned} \quad (16)$$

Here, D_p is the diffusion coefficient of the nanopowder [47], which can be rewritten as

$$D_p = \frac{k_B T}{3\pi \eta d_v} \left(g^{-1/3} + 3.314 \frac{l}{d_v} g^{-2/3} \right), \quad (17)$$

where d denotes the diameter and l stands for the mean free path. D_v is the diffusion coefficient of material vapor obtained from the second viscosity approximation in the literature [48]. K_{th} is the thermophoresis coefficient [49].

3. Expressing Turbulent Effects

3.1. Approximations for eddy diffusivity A turbulent flow comprises multiscale eddies interacting with each other incessantly. As discussed in the literature [35], a high-temperature argon plasma flow cannot have sub-millimeter eddies, whereas a low-temperature argon flow can have eddies larger than sub-millimeters. Simulation of a turbulent flow of a thermal plasma interacting with a nonionized cold gas requires a theoretical model that can treat such a flow field of multiscale eddies.

Simulation without turbulence models is called direct numerical simulation (DNS), which simulates a turbulent flow by capturing every eddy with a grid element size that is much smaller than the minimum eddy size. Because of the limitations of computational time and resources, DNS with satisfactory quality is generally arduous, even for normal fluid flows.

Therefore, thermal plasma flow simulations should practically assimilate turbulence models to express the important nature. In the last three decades, Reynolds-averaged Navier–Stokes (RANS) models such as the standard $k-\varepsilon$ model [50] have been adopted in many simulations [51–68]. It is noteworthy, however, that the standard $k-\varepsilon$ model is an empirical model for a turbulent flow of a normal fluid with a constant kinematic viscosity. Thermal plasma flows always have variable kinematic viscosities because of large temperature variations. To overcome this problem, the Re-normalization group (RNG) $k-\varepsilon$ model [69] was applied to the simulation of a DC transferred arc plasma in a twin-torch system [70]. The Reynolds stress model [71] was also adopted to investigate turbulent effects on nanopowder production using a radio frequency inductively coupled thermal plasma [33].

Large eddy simulation (LES) approaches have been a recent trend for thermal plasma flow simulations [6,72–82]. LES is a time-dependent approach that deals with dynamic motions of large eddies directly using a grid system and models only turbulence composed of small eddies, unresolved by the grid element size. Therein, by low-pass-filtering operations, the governing equations are transformed into similar forms with the numerically solvable terms at the large grid scale (GS) and the eddy–diffusivity terms at the sub-grid scale (SGS). That is, the following terms, which express diffusive effects due to eddies at the SGS, are added to the right-hand sides of the governing equations. It should be noted that, after the transformation, the variables on the left-hand sides are not the original ones any more but are the filtered ones, although they look like the same forms. The detailed discussion is found in the literature [35].

On the basis of the Smagorinsky model [83] with the filter width $\bar{\Delta}$ and the model parameters C_I and C_S , the eddy–diffusive effect of momentum at the SGS was proposed as [84]

$$-\nabla \cdot \boldsymbol{\tau}^{\text{SGS}} = -\nabla \cdot \left\{ \frac{4}{3} C_I \bar{\Delta}^2 \bar{\rho} (\tilde{\mathbf{S}} : \tilde{\mathbf{S}}) \mathbf{I} - C_S^2 \bar{\Delta}^2 \bar{\rho} \sqrt{2 (\tilde{\mathbf{S}} : \tilde{\mathbf{S}})} \left[2\tilde{\mathbf{S}} - \frac{2}{3} (\nabla \cdot \tilde{\mathbf{u}}) \mathbf{I} \right] \right\} \quad (18)$$

which is an example of SGS stresses and added to the right-hand side in (2). The symbols $\bar{\cdot}$ and $\tilde{\cdot}$ on the variables denote ‘low-pass-filtered’ and ‘density-weighted-averaged’. The eddy–diffusive effect of energy at the SGS might be written as

$$-\nabla \cdot \mathbf{q}^{\text{SGS}} = -\nabla \cdot \left[-\frac{C_S^2 \bar{\Delta}^2 \bar{\rho} \sqrt{2 (\tilde{\mathbf{S}} : \tilde{\mathbf{S}})}}{\text{Pr}_T} \nabla \tilde{h} \right] \quad (19)$$

which is added to the right-hand side in (3). Pr_T is the turbulent Prandtl number, which is obtainable dynamically [85]. The terms related to the pressure gradient and viscous dissipation at the SGS

$$\Pi^{\text{SGS}} = \overline{(\mathbf{u} \cdot \nabla) P} - (\tilde{\mathbf{u}} \cdot \nabla) \bar{P} \quad (20)$$

and

$$\varepsilon^{\text{SGS}} = C_S^2 \bar{\Delta}^2 \bar{\rho} \sqrt{2 (\tilde{\mathbf{S}} : \tilde{\mathbf{S}})} \left[2 (\tilde{\mathbf{S}} : \tilde{\mathbf{S}}) - \frac{2}{3} (\nabla \cdot \tilde{\mathbf{u}})^2 \right] \quad (21)$$

are also added to the right-hand side in (3). However, for thermal plasma flows, these terms still remain unclear.

The smallest scale of eddies is presumed to be 0.01 mm or larger [35,78], which is much larger than the scales of nanoparticles and vapor molecules. That effect works fairly well on both nanoparticles and vapor molecules. Therefore, the eddy–diffusive effect of nanoparticles and vapor molecules at the SGS can be written as

$$-\nabla \cdot \mathbf{J}_p^{\text{SGS}} = -\nabla \cdot \left[-\frac{C_S^2 \bar{\Delta}^2 \bar{\rho} \sqrt{2 (\tilde{\mathbf{S}} : \tilde{\mathbf{S}})}}{\text{Sc}_T} \nabla \left(\frac{\tilde{n}_p}{\bar{\rho}} \right) \right], \quad (22)$$

$$-\nabla \cdot \mathbf{J}_f^{\text{SGS}} = -\nabla \cdot \left[-\frac{C_S^2 \bar{\Delta}^2 \bar{\rho} \sqrt{2 (\tilde{\mathbf{S}} : \tilde{\mathbf{S}})}}{\text{Sc}_T} \nabla \left(\frac{\tilde{f}}{\bar{\rho}} \right) \right], \quad (23)$$

and

$$-\nabla \cdot \mathbf{J}_v^{\text{SGS}} = -\nabla \cdot \left[-\frac{C_S^2 \bar{\Delta}^2 \bar{\rho} \sqrt{2 (\tilde{\mathbf{S}} : \tilde{\mathbf{S}})}}{\text{Sc}_T} \nabla \left(\frac{\tilde{n}_v}{\bar{\rho}} \right) \right], \quad (24)$$

which are added to the right-hand side in (14)–(16), respectively. A constant value of 0.9 is given to the turbulent Schmidt number Sc_T , as investigated in many studies reported in the literature [86].

The model parameters C_I and C_S are usually constants in standard Smagorinsky-type models, whereas those parameters can be determined dynamically by various approaches [87–91]. Thermal plasma flow simulations are capable of treating simultaneously laminar (nonturbulent) regions with high kinematic viscosity and turbulent regions with low kinematic viscosity in and around a plasma. To satisfy this condition, the demonstrative simulations in Section 4 are performed with the coherent structure model [90,91] to obtain C_S dynamically. It is noteworthy that filter shapes do not make much of a difference, although filter widths affect numerical solutions considerably in Smagorinsky-type models.

3.2. Numerical methods The thermal flow field, in which a plasma over 10 000 K and nonionized gas at 300 K coexist, is treated simultaneously during computation. Its widely ranging temperature causes large variations of the transport properties and density with several orders of magnitude. Meanwhile, the Mach number is on the order of 10^{-3} – 10^{-1} . Therefore, to obtain the solution in a practically sufficient timescale, such a partially ionized gas flow is treated as an incompressible flow with a temperature-dependent density. Therefore, the following requirements should be satisfied in numerical methods:

- (A) Small eddies are resolved with a large grid element size to reduce computational costs.
- (B) Steep gradients of variables are also captured by the grid element size.
- (C) The discretization errors are small even with the large grid element size.
- (D) The time-integration errors are small even with a large time increment.
- (E) A solution algorithm for incompressible flows is preferable even with large density variation.
- (F) Computation is robust even with large variations of density and transport properties.

Requirements (D), (E), and (F) are important to perform sufficiently long computation to obtain statistical information of turbulence by evaluating numerous eddy motions. However, with a

Table I. Numerical methods for demonstrative simulations

	Conventional	Present
Algorithm	SIMPLE	IPISO
Convection terms	Upwind scheme with 1st-order accuracy	Hybrid-upwind K-K scheme with mainly 3rd-order accuracy
Transient terms	Euler scheme with 1st-order accuracy	Adams-Bashforth-Moulton scheme with 3rd-order accuracy
Diffusion terms		Central differencing scheme with 2nd-order accuracy
Source terms		Central differencing scheme with 2nd-order accuracy

method for incompressible flows, simulations of a flow with large variations of density and transport properties tend to experience easy breakdown of computation.

Table I presents two numerical methods used in the demonstrative simulations. The conventional method has often been used for thermal plasma flow simulations because it obtains a numerical solution relatively easily even for that computationally severe condition. It adopts the semi-implicit method for pressure linked equations (SIMPLE) algorithm [92] with the upwind differencing scheme with the first-order accuracy for the convection terms and the Euler differencing scheme with the first-order accuracy for the transient terms. The present method adopts the improved pressure implicit with splitting of operator (IPISO) algorithm [93] with the hybrid upwind Kawamura–Kuwahara scheme with the third-order accuracy [94] for the convection terms and the Adams–Bashforth–Moulton scheme with the third-order accuracy [95] for the transient terms. This method is expected not only to express turbulent features but also to perform stable computation even with a large increment of time steps. More discussion about differencing schemes and solution algorithms can be found in the literature [35].

4. Demonstrative Simulations

4.1. Computational conditions A two-dimensional simulation is sufficiently useful for the present discussion because a two-dimensional forming field represents an elemental structure comprising an actual three-dimensional turbulent field. Figure 1 illustrates an argon thermal plasma jet ejected into an argon atmosphere from the nozzle. The computational domain is fixed in a two-dimensional axisymmetric coordinate system. The origin is located at the center of the exit of the nozzle with the inner radius r_{wall} of 4.0 mm. z and r denote the axial and radial positions, respectively. Based on the measurement results [96], the radial profiles of the axial velocity u_{nozzle} and temperature T_{nozzle} at the nozzle exit are given as the following polynomials:

$$u_{\text{nozzle}} = 150 + 33 \left(\frac{r}{r_{\text{wall}}} \right) - 614 \left(\frac{r}{r_{\text{wall}}} \right)^2 + 928 \left(\frac{r}{r_{\text{wall}}} \right)^3 - 480 \left(\frac{r}{r_{\text{wall}}} \right)^4 \quad (25)$$

and

$$T_{\text{nozzle}} = 10400 - 10500 \left(\frac{r}{r_{\text{wall}}} \right) + 33533 \left(\frac{r}{r_{\text{wall}}} \right)^2 - 64000 \left(\frac{r}{r_{\text{wall}}} \right)^3 + 33067 \left(\frac{r}{r_{\text{wall}}} \right)^4 \quad (26)$$

as shown in Fig. 2. These profiles are stationary boundary conditions at the inlet of the computational domain because this discussion excludes the effect of disturbances from arc restriking in the nozzle, as described in Sections 1.2 and 2.1. The nonslip condition is imposed on the nozzle surface with 300 K. At the outlet boundary of the computational domain, Neumann conditions are applied to all variables, satisfying conservation of the mass flow [97]. As a precursor material, silicon vapor is supplied at 0.1 g min^{-1} with the plasma jet. The density of silicon vapor is negligibly

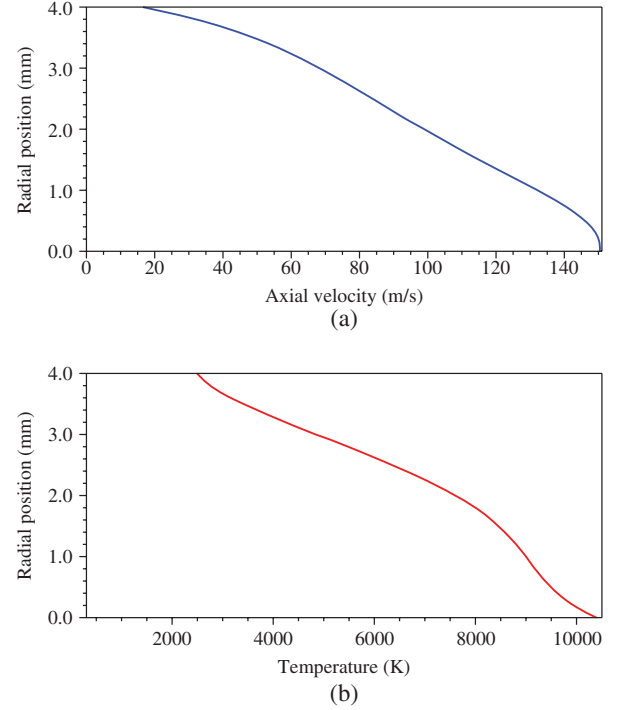


Fig. 2. Plasma jet profiles at the nozzle exit: (a) axial velocity, and (b) temperature

small compared to that of the argon plasma flow. The momentum exchange at nanopowder generation is also neglected because the mass flow rate of the raw material is much less than that of argon gas under typical conditions of thermal plasma processing.

For the thermal plasma jet, the Reynolds number based on the nozzle diameter is $145\text{--}3849$, which predicts that the plasma jet cannot keep a laminar state but will easily experience turbulence transition [40]. Therefore, to resolve multiscale eddies, a staggered grid system is used with discrete points having a uniform interval of $\Delta r = \Delta z = 0.1 \text{ mm}$ in both radial and axial directions. However, because smaller eddies that cannot be resolved even by this interval might exist, an LES approach is adopted to take account of their eddy-diffusive effects in the SGS described by (18)–(23) with the filter width defined as $\Delta = (r\Delta r\Delta z)^{1/3}$. The first term of the right-hand side in (18) is neglected. The parameter C_S is determined dynamically by the coherent structure model [90,91]. The time increment is set as 0.1 ms .

The temperature-dependent thermodynamic and transport properties of argon, which include the effects of ionization in LTE, are implemented [1]. The temperature-dependent radiation is obtained from the literature [98]. The material properties of silicon are obtained from the database [99].

It should be noted that an eddy represents a vortex ring around the central axis of a two-dimensional axisymmetric frame. An actual turbulent flow includes eddies whose axes are oriented three dimensionally in various directions. Because LES is a model approximating such a feature, it should generally be applied to three-dimensional simulation. Furthermore, the filter width varies depending on the radial position r , although it affects numerical

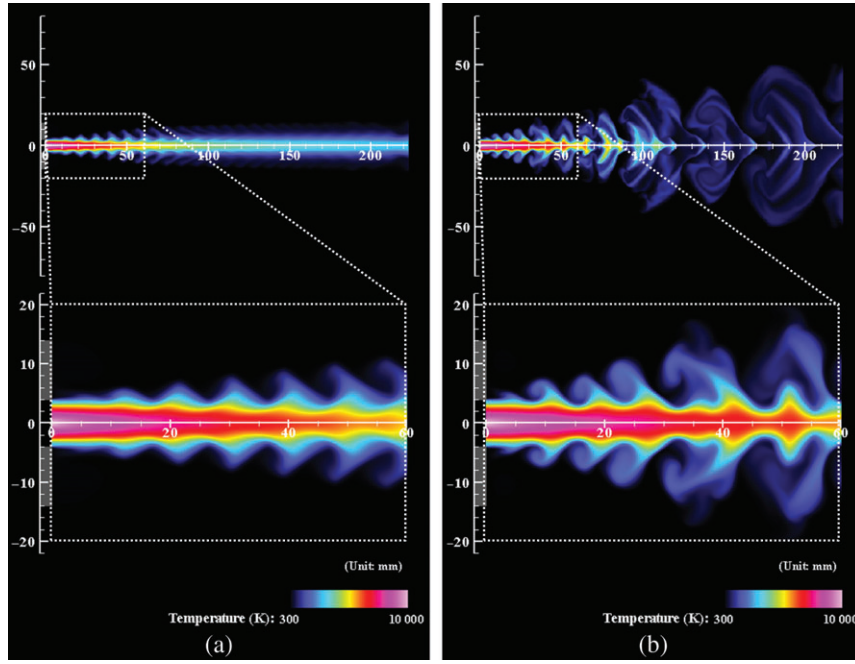


Fig. 3. Instantaneous temperature fields obtained by (a) the conventional model, and (b) the present model. (See also animation on <http://masayashigeta.com/IEEJ2018/IEEJ2018.html>)

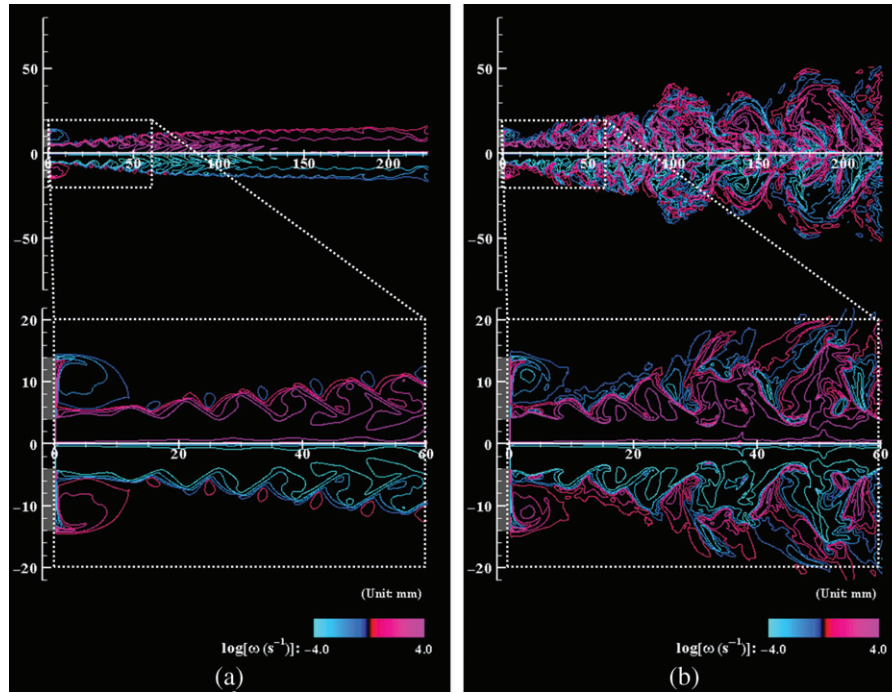


Fig. 4. Instantaneous vorticity fields obtained by (a) the conventional model, and (b) the present model. (See also animation on <http://masayashigeta.com/IEEJ2018/IEEJ2018.html>)

results. However, no benchmark data based on experiments or DNS are available to evaluate the model parameters quantitatively for turbulence in thermal plasma flows. It is limited to qualitative discussion. Nevertheless, because the present frame work can highlight the elemental structures that appear locally in an actual thermal flow, it is still acceptable at present.

4.2. Numerical results of the thermal plasma jet

Figures 3 and 4 show snapshots of the instantaneous temperature and vorticity fields, respectively. (See also the corresponding animations in the author's website <http://masayashigeta.com/IEEJ2018/IEEJ2018.html>.) It is apparent that the present method simulates the entrainment of ambient low-temperature gas into the

high-temperature plasma jet with eddy motions. Furthermore, the vorticity field indicates the following process: Eddies are first generated at the interfacial region between the plasma jet and ambient nonionized gas by Kelvin–Helmholtz instability. Flowing downstream, they induce other eddies and simultaneously break themselves up into smaller eddies. Consequently, the vorticity field becomes complex with multiscale eddies. These features of a thermal plasma jet were also observed in an experiment in an earlier report [34]. The vorticity fields were expressed by contour lines of

$$\Omega_{\omega} = \begin{cases} \log |\omega| & (\text{for } \omega > 0) \\ -\log |\omega| & (\text{for } \omega < 0) \end{cases} \quad (27)$$

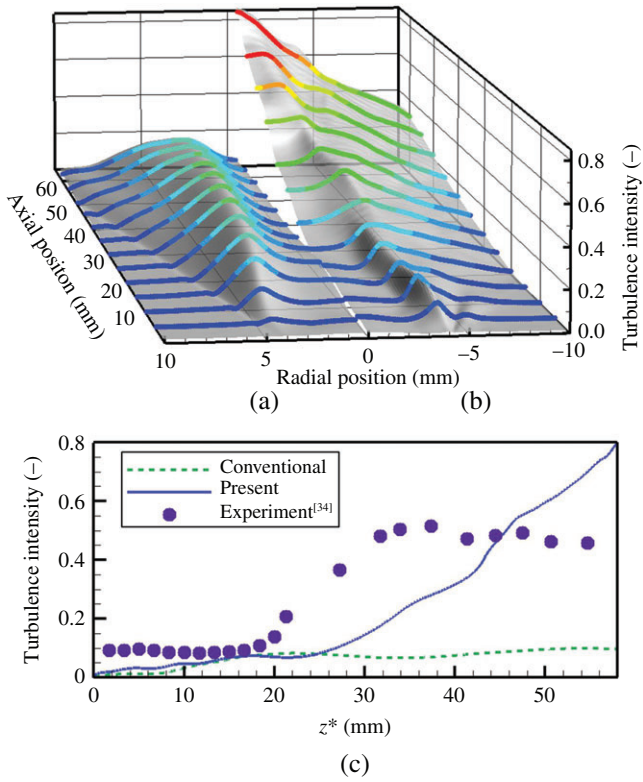


Fig. 5. Turbulence intensity distributions obtained by (a) the conventional model, (b) the present model, and (c) axial profile comparison with experiment [34]

with the interval of 0.5 for $\log|\omega| \geq 2.5$. Here, ω stands for the vorticity with a unit of s^{-1} . Positive and negative Ω_ω denote anticlockwise and clockwise rotations, respectively.

Compared to the present method using the IPISO algorithm and the differencing schemes with higher order accuracy for convection and transient terms, the conventional method using the SIMPLE algorithm and the conventional differencing schemes

with first-order accuracy does not simulate the features of a thermal plasma jet. Although eddies are generated and entrainment almost occurs in the upstream region, they attenuate in the downstream region because the upwind differencing scheme with the first-order accuracy for the convection terms inherently includes a large discretization error that unphysically flattens the spatial gradients of variables. Therefore, the gradient of temperature is also blurred and the eddies disappear by the nonphysical diffusional effects.

Indeed, the turbulence intensity profile in Fig. 5 shows the same tendency as that obtained by the experiment [34]. Here, both turbulence intensities were defined in the same manner as the ratio of the standard deviation of the axial fluctuating velocity for a given data location divided by the centerline mean velocity for the same given axial distance downstream. For comparison, in Fig. 5(c), the horizontal axis shows a modified axial position $z^* = z \times (u_{\text{nozzle}[\text{max}]}/150)$, where $u_{\text{nozzle}[\text{max}]}$ is 150 m s^{-1} for the simulations or 400 m s^{-1} for the experiment [34] with consideration of the velocity difference at the nozzle exit. It is reasonable that the thermal plasma jet in the experiment tends to transition from a laminar flow into a turbulent flow in a more upstream region than that in the present simulation without any disturbances at the nozzle exit because an actual thermal plasma jet includes disturbances caused by arc restriking inside the nozzle. Although they have some discrepancies, as described in Sections 2.1 and 4.1, the present results indicate the elemental structures and fundamental mechanisms in actual three-dimensional processes. Therefore, the present results can be used validly for qualitative discussion at least.

4.3. Numerical results of the nanopowder

Figure 6 shows snapshots of the instantaneous number density distributions of silicon vapor molecules at the same moment as Figs. 3 and 4. Moreover, Figs. 7 and 8 show snapshots of the instantaneous number density and mean diameter distributions of silicon nanoparticles at the same moment. (See also the corresponding animations in the author's website <http://masayashigeta.com/IEEJ2018/IEEJ2018.html>.)

The vapor ejected from the jet nozzle is transported mainly by plasma jet convection. At the same time, the vapor diffuses by its

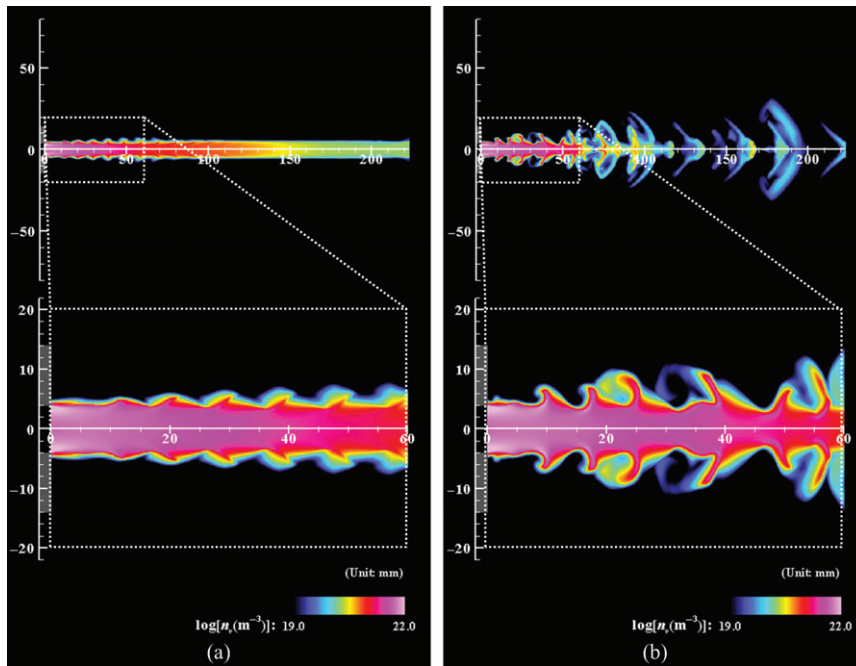


Fig. 6. Instantaneous number density distributions of vapor molecules obtained by (a) the conventional model, and (b) the present model. (See also animation on <http://masayashigeta.com/IEEJ2018/IEEJ2018.html>)

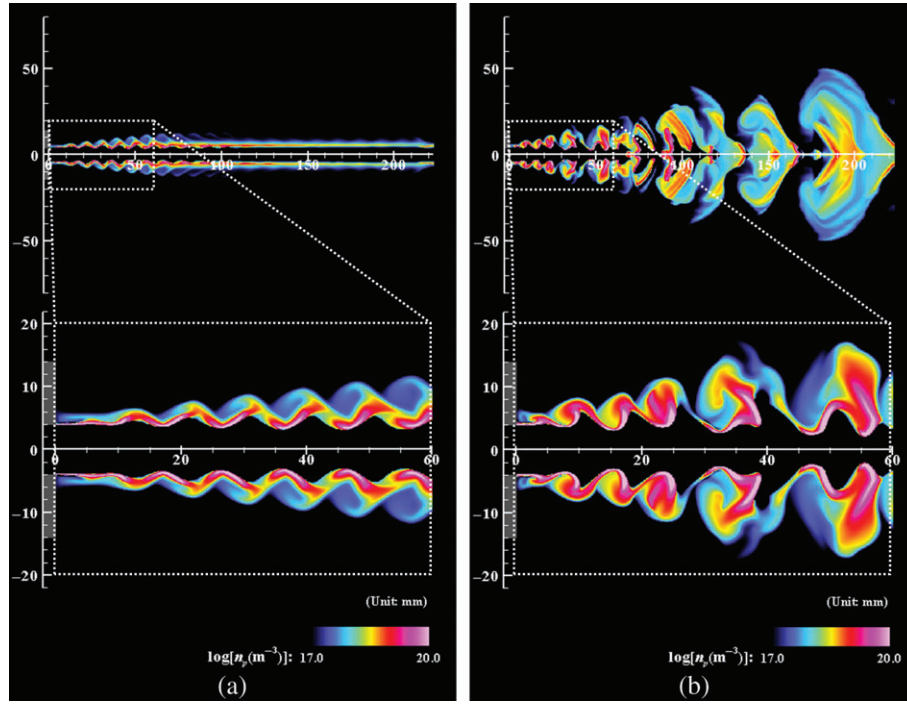


Fig. 7. Instantaneous number density distributions of nanoparticles obtained by (a) the conventional model and (b) the present model. (See also animation on <http://masayashigeta.com/IEEJ2018/IEEJ2018.html>)

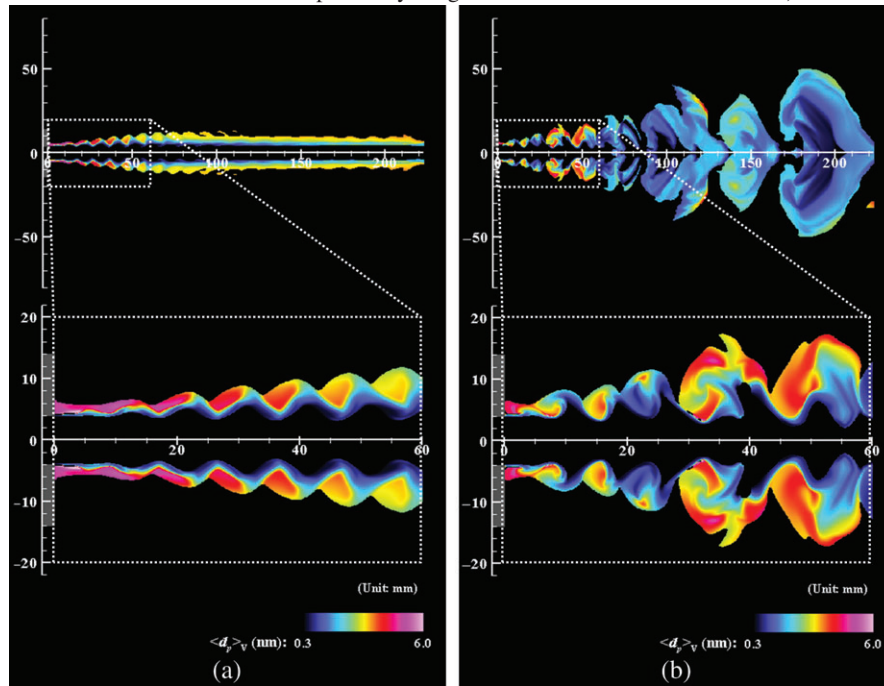


Fig. 8. Instantaneous mean diameter distributions of nanoparticles obtained by (a) the conventional model, and (b) the present model. (regions for $n_p < 10^{17} \text{ m}^{-3}$ are cut off.). (See also animation on <http://masayashigeta.com/IEEJ2018/IEEJ2018.html>)

own gradient crossing the plasma's fringe, where the vapor experiences a temperature decrease. As a result, it becomes supersaturated and changes its phase to nanoparticles through nucleation, condensation, and coagulation. Therefore, a large number of small nanoparticles exist at the plasma fringe. Because the nanoparticles grow up collectively and diffuse outside the plasma region, they distribute widely in the field. The larger mean diameter regions in Fig. 8 coincide with smaller number density regions in Fig. 7. This result indicates that simultaneous coagulation decreasing the particle number plays a significant role for nanopowder growth as well.

The simulations exhibit the mean diameters ranging from sub-nanometers to 6 nm. This size range seems reasonable. Several

experimental studies have actually reported that nanopowders produced by thermal plasmas had widely dispersed size distributions ranging from a few to a few tens of nanometers although different types of thermal plasmas were used [16,18,100–104]. For instance, Rao *et al.* [101] produced silicon nanopowder by a DC thermal plasma jet combined with a unique quenching system. They determined the size of the nanopowder using a scanning electrical mobility spectrometer, which could detect particles larger than 4 nm. As a result, excluding particles smaller than 4 nm, the mean diameter of their nanopowder was approximately 8.5 nm; and 90% of the particles were smaller than 16 nm. Berlinger *et al.* [104] fabricated iron-based nanopowder by a thermal plasma in gas-metal-arc welding and measured the particle diameters from

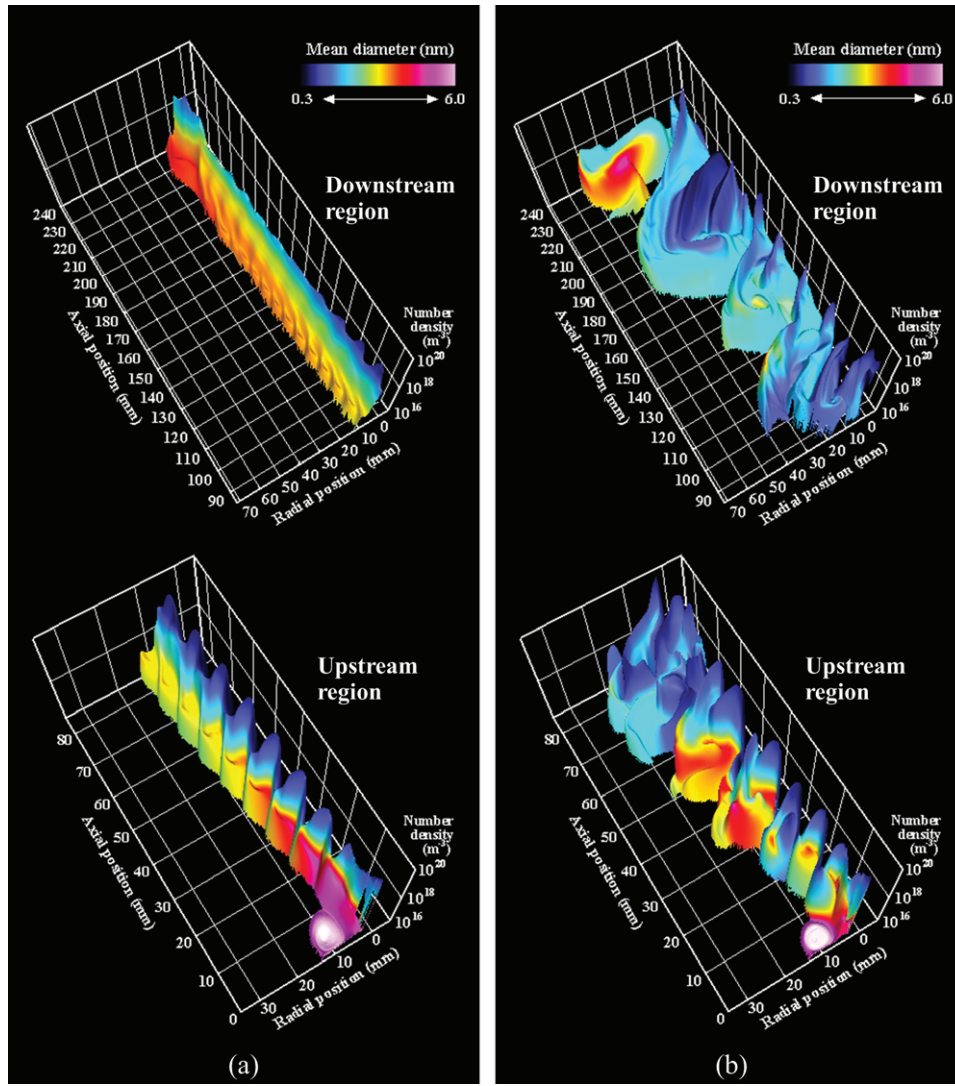


Fig. 9. Combined expressions of the nanopowder's number density and mean diameter distributions in a three-dimensional frame obtained by (a) the conventional model and (b) the present model. (See also animation on <http://masayashigeta.com/IEEJ2018/IEEJ2018.html>)

transmission electron microscopy images. They showed that 80% of the nanoparticles were smaller than 10 nm. Shigeta and Watanabe [16,18] reported that silicon-based compound nanopowders produced by an induction thermal plasma had diameters ranging from 2 to 20 nm approximately. The mean diameters predicted by the present simulations are in those practical ranges. It should be stressed that particle diameters smaller than a few nanometers cannot be measured usually in experiments even if such small nanoparticles are produced.

It is also obvious that the conventional method and the present method give very different results, although the governing equations, the boundary conditions, and the given parameters are the same. As discussed in the previous section, the conventional method blurs gradients of the variables. As a result, the vapor and the nanopowder experience unphysically large diffusion. Note, those methods give very different temperature and flow fields, which cause the differences of the vapor and nanopowder fields as well.

Figure 9 displays the combined expressions of the nanopowder's number density and mean diameter distributions in a three-dimensional frame. The upper and lower figures depict the downstream and upstream regions, respectively. Steep cliffs of small particles are generated continuously at the plasma fringes. On the other hand, the valleys between the cliffs show large particles. These features indicate the following growth process:

Numerous sub-nanometer particles are generated by nucleation and condensation in the thin layers near the plasma jet. Those particles diffuse into the valleys and there increase their size, decreasing their number by coagulation. Both numerical methods obtain such 'cliff-valley structures' in the upstream region. Traveling downstream, the structures begin to deform at around 70 mm away from the nozzle exit. The conventional method predicts that the structure transforms into a 'wall' in the downstream region, whereas the present model predicts that the structure changes to a 'canyon'.

Experimental results support the validity of the present simulations, which obtain the same scale of particle sizes. However, no experimental evidence exists to support the dynamically transformed distribution of nanopowder as shown in this paper. Some technological breakthrough is expected to support its investigation on an experimental basis.

4.4. Correlation between plasma flow and nanopowder generation

Nanopowder is generated after the material vapor experiences supersaturation during a temperature decrease at the plasma fringe, at which small temperature fluctuations are also generated by fluid-dynamic instability. The fluctuations grow with eddies and finally form a complex temperature field, as shown in Fig. 3. It is readily conjectured that the downstream nanopowder

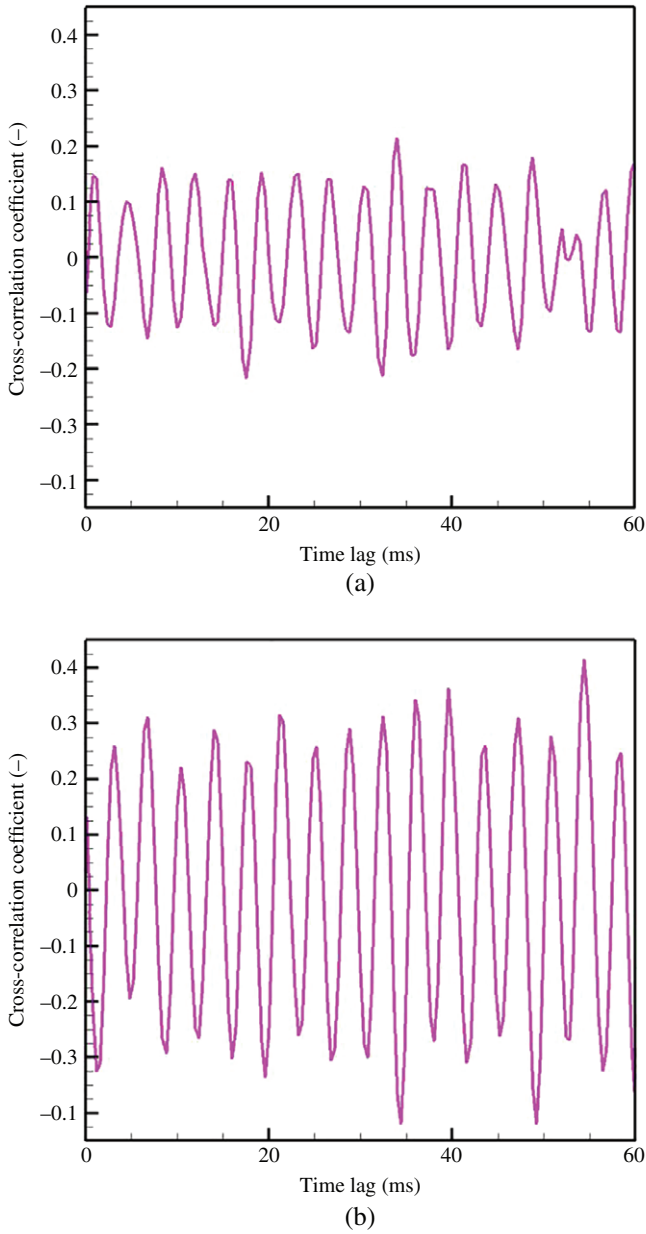


Fig. 10. Cross-correlation coefficients between temperature fluctuation at $(z_0, r_0) = (10 \text{ mm}, 4 \text{ mm})$ and nanopowder's number density fluctuation at (a) $(z, r) = (55 \text{ mm}, 4 \text{ mm})$ and (b) $(z, r) = (55 \text{ mm}, 14 \text{ mm})$ obtained by the present model

distribution starts from and therefore responds to the upstream temperature fluctuations. To analyze this feature, the cross-correlation between these two factors was evaluated. Specifically, the cross-correlation coefficients for the fluctuations of temperature at a fixed position and the number density of nanoparticles were calculated as

$$R_{\text{cross}}(\tau, z, r) = \frac{\int_{t_0}^{t_1} T'(t, z_0, r_0) \cdot n_p'(t + \tau, z, r) dt}{\sqrt{\int_{t_0}^{t_1} |T'(t, z_0, r_0)|^2 dt} \cdot \sqrt{\int_{t_0}^{t_1} |n_p'(t, z, r)|^2 dt}} \quad (28)$$

using quasi-periodic data during 102.4 ms ($= t_1 - t_0$). Here, τ is the time lag. The prime mark denotes the fluctuation, defined as the difference from the time-averaged value. The fixed position $(z_0, r_0) = (10 \text{ mm}, 4 \text{ mm})$ was selected as an anchoring point in the upstream region.

Figure 10(a) and (b) show examples of the cross-correlation coefficients obtained for the fluctuations of number density of

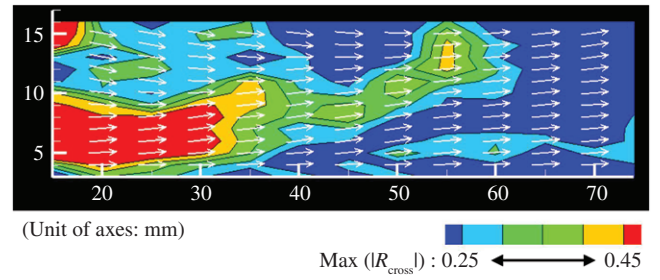


Fig. 11. Map of the maximum cross-correlation coefficients between temperature fluctuation at $(z_0, r_0) = (10 \text{ mm}, 4 \text{ mm})$ and nanopowder's number density fluctuation at each position and time-averaged flow-direction vectors obtained by the present model

nanoparticles at $(z, r) = (55 \text{ mm}, 4 \text{ mm})$ and $(z, r) = (55 \text{ mm}, 14 \text{ mm})$, respectively. Figure 11 shows a map of the maximum values of the cross-correlation coefficient magnitude obtained at each position. The time-averaged flow direction vectors are shown as well. Their lengths are equal, indicating only the flow directions. It is readily apparent that the dynamic behavior of the nanopowder distribution is closely correlated with the small temperature fluctuation in the upstream region. The closer positions have stronger correlations, which seems natural. It is interesting that the influence at $(z_0, r_0) = (10 \text{ mm}, 4 \text{ mm})$ propagates not in the flow direction but in a direction away from the plasma jet axis. For example, focusing on the row along $z = 55 \text{ mm}$, the positions at $r = 12\text{--}14 \text{ mm}$ exhibit stronger correlations than those at $r = 4\text{--}11 \text{ mm}$. This result suggests that the distribution of growing nanopowder not near but distant from a plasma jet can be controlled via control of the temperature fluctuation at the upstream plasma fringe.

5. Summary and Conclusions

This paper discussed theoretical models and numerical methods to simulate a turbulent thermal plasma jet transporting a nanopowder. In addition to the thermal plasma jet model, a sophisticated model was described mathematically for nanopowder's collective growth by homogeneous nucleation, heterogeneous condensation, and coagulation among nanoparticles, and also transport by convection, diffusion, and thermophoresis simultaneously. Demonstrative simulations visualized the dynamically forming fields of both the plasma jet with multiscale eddies and the nanopowder. Although it was restricted in two dimensions, the obtained two-dimensional field represents elemental structures constituting an actually three-dimensional turbulent field. The noteworthy results are summarized as follows:

1. Suitable solution algorithms and differencing schemes with high-order accuracy should be used for long and robust simulation capturing multiscale eddies and steep gradients of temperature, which are turbulent features of thermal plasma flows with locally variable density, transport properties, and Mach numbers.
2. Eddies are first generated at the interfacial region between the plasma jet and ambient nonionized gas by fluid-dynamic instability. Flowing downstream, they induce other eddies and simultaneously break themselves up into smaller eddies. As a result, the vorticity field becomes complex with multiscale eddies. Because of those generation-breakup process of eddies, the plasma flow entrains the ambient cold gas and deforms its shape traveling downstream.
3. Numerous sub-nanometer particles are generated by nucleation and condensation in the thin layers near the plasma jet. Those particles diffuse and increase their size, decreasing their number by coagulation. In a three-dimensional frame that expresses the number density and mean diameter of nanoparticles simultaneously, a

‘cliff–valley structure’ is formed in the upstream region; traveling downstream, the structure changes to a ‘canyon’.

4. The dynamic behavior of the nanopowder distribution is correlated closely with the slight temperature fluctuation in the upstream region. That upstream influence propagates not in the flow direction but in a direction away from the plasma jet. This result suggests that the nanopowder distribution distant from a plasma jet can be controlled via the control of the temperature fluctuation at the upstream plasma fringe.

Acknowledgments

This work was partly supported by a Japan Society for the Promotion of Science (JSPS) Grant-in-Aid for Challenging Exploratory Research (KAKENHI: Grant no. 16K13737).

References

- (1) Boulos MI, Fauchais P, Pfender E. *Thermal Plasmas Fundamentals and Applications*, vol. 1. Plenum Press: New York; 1994.
- (2) Sato T, Shigeta M, Kato D, Nishiyama H. Mixing and magnetic effects on a nonequilibrium argon plasma jet. *International Journal of Thermal Sciences* 2001; **40**:273–278.
- (3) Shigeta M, Sato T, Nishiyama H. Computational simulation of a particle-laden RF inductively coupled plasma with seeded potassium. *International Journal of Heat and Mass Transfer* 2004; **47**:707–716.
- (4) Shigeta M, Nishiyama H. Numerical analysis of metallic nanoparticle synthesis using RF inductively coupled plasma flows. *Journal of Heat Transfer* 2005; **127**:1222–1230.
- (5) Tanaka Y, Muroya Y, Hayashi K, Uesugi Y. Simultaneous control of numerical enhancement of N atoms and decrease in heat flux into reaction chamber using Ar–N₂ pulse-modulated induction thermal plasmas. *Applied Physics Letters* 2006; **89**:031501.
- (6) Shigeta M. Numerical study of axial magnetic effects on a turbulent thermal plasma jet for nanopowder production using 3D time-dependent simulation. *Journal of Flow Control, Measurement & Visualization* 2018; **6**:107–123.
- (7) Mostaghimi J, Boulos MI. Thermal plasma sources: How well are they adopted to process needs? *Plasma Chemistry and Plasma Processing* 2015; **35**:421–436.
- (8) Fauchais P. Understanding plasma spraying. *Journal of Physics D: Applied Physics* 2004; **37**:R86–R108.
- (9) Heberlein J, Murphy AB. Thermal plasma waste treatment. *Journal of Physics D: Applied Physics* 2008; **41**:053001.
- (10) Murphy AB, Tanaka M, Yamamoto K, Tashiro S, Sato T, Lowke JJ. Modelling of thermal plasmas for arc welding: The role of the shielding gas properties and of metal vapour. *Journal of Physics D: Applied Physics* 2009; **42**:194006.
- (11) Colombo V, Concetti A, Ghedini E, Dallavalle S, Vancini M. High-speed imaging in plasma arc cutting: a review and new developments. *Plasma Sources Science and Technology* 2009; **18**:023001.
- (12) Shigeta M, Murphy AB. Thermal plasmas for nanofabrication. *Journal of Physics D: Applied Physics* 2011; **44**:174025.
- (13) Siegel RW. Synthesis and properties of nanophase materials. *Materials Science and Engineering: A* 1993; **168**:189–197.
- (14) Watanabe T, Nezu A, Abe Y, Ishii Y, Adachi K. Formation mechanism of electrically conductive nanoparticles by induction thermal plasmas. *Thin Solid Films* 2003; **435**:27–32.
- (15) Watanabe T, Okumiyama H. Formation mechanism of silicide nanoparticles by induction thermal plasmas. *Science and Technology of Advanced Materials* 2004; **5**:639–646.
- (16) Shigeta M, Watanabe T. Growth mechanism of silicon-based functional nanoparticles fabricated by inductively coupled thermal plasmas. *Journal of Physics D: Applied Physics* 2007; **40**:2407–2419.
- (17) Ryu T, Sohn HY, Hwang KS, Fang ZZ. Chemical vapor synthesis (CVS) of tungsten nanopowder in a thermal plasma reactor. *International Journal of Refractory Metals & Hard Materials* 2009; **27**:149–154.
- (18) Shigeta M, Watanabe T. Effect of precursor fraction on silicide nanopowder growth under thermal plasma conditions: A computational study. *Powder Technology* 2016; **288**:191–201.
- (19) Tanaka Y, Tsuke T, Guo W, Uesugi Y, Ishijima T, Watanabe S, Nakamura K. A large amount synthesis of nanopowder using modulated induction thermal plasmas synchronized with intermittent feeding of raw materials. *Journal of Physics: Conference Series* 2012; **406**:012001.
- (20) Kodama N, Tanaka Y, Kita K, Uesugi Y, Ishijima T, Watanabe S, Nakamura K. A method for large-scale synthesis of Al-doped TiO₂ nanopowder using pulse-modulated induction thermal plasmas with time-controlled feedstock feeding. *Journal of Physics D: Applied Physics* 2014; **47**:195304.
- (21) Kambara M, Kitayama A, Homma K, Hideshima T, Kaga M, Sheem K-Y, Ishida S, Yoshida T. Nano-composite Si particle formation by plasma spraying for negative electrode of Li ion batteries. *Journal of Applied Physics* 2014; **115**:143302.
- (22) Girshick SL, Chiu C-P, Munro R, Wu CY, Yang L, Singh SK, McMurtry PH. Thermal plasma synthesis of ultrafine iron particles. *Journal of Aerosol Science* 1993; **24**:367–382.
- (23) Bilodeau JF, Proulx P. A mathematical model for ultrafine iron powder growth in thermal plasma. *Aerosol Science and Technology* 1996; **24**:175–189.
- (24) Desilets M, Bilodeau JF, Proulx P. Modelling of the reactive synthesis of ultra-fine powders in a thermal plasma reactor. *Journal of Physics D: Applied Physics* 1997; **30**:1951–1960.
- (25) Cruz ACD, Munz RJ. Vapor phase synthesis of fine particles. *IEEE Transactions on Plasma Sciences* 1997; **25**:1008–1016.
- (26) Aristizabal F, Munz RJ, Berk D. Modeling of the production of ultra fine aluminium particles in rapid quenching turbulent flow. *Journal of Aerosol Science* 2006; **37**:162–186.
- (27) Goortani BM, Proulx P, Xue S, Mendoza-Gonzalez NY. Controlling nanostructure in thermal plasma processing: Moving from highly aggregated porous structure to spherical silica nanoparticles. *Powder Technology* 2007; **175**:22–32.
- (28) Mendoza-Gonzalez NY, Goortani BM, Proulx P. Numerical simulation of silica nanoparticles production in an RF plasma reactor: Effect of quench. *Materials Science and Engineering: C* 2007; **27**:1265–1269.
- (29) Shigeta M, Watanabe T. Numerical investigation of cooling effect on platinum nanoparticle formation in inductively coupled thermal plasmas. *Journal of Applied Physics* 2008; **103**:074903.
- (30) Shigeta M, Watanabe T. Two-dimensional analysis of nanoparticle formation in induction thermal plasmas with counterflow cooling. *Thin Solid Films* 2008; **516**:4415–4422.
- (31) Vorobev A, Zikanov O, Mohanty P. Modelling of the in-flight synthesis of TaC nanoparticles from liquid precursor in thermal plasma jet. *Journal of Physics D: Applied Physics* 2008; **41**:085302.
- (32) Vorobev A, Zikanov O, Mohanty P. A co-condensation model for in-flight synthesis of metal-carbide nanoparticles in thermal plasma jet. *Journal of Thermal Spray Technology* 2008; **17**:956–965.
- (33) Colombo V, Ghedini E, Gherardi M, Sanibondi P, Shigeta M. A two-dimensional nodal model with turbulent effects for the synthesis of Si nano-particles by inductively coupled thermal plasmas. *Plasma Sources Science and Technology* 2012; **21**:025001.
- (34) Pfender E, Fincke J, Spores R. Entrainment of cold gas into thermal plasma jets. *Plasma Chemistry and Plasma Processing* 1991; **11**:529–543.
- (35) Shigeta M. Turbulence modelling of thermal plasma flows. *Journal of Physics D: Applied Physics* 2016; **49**(49):493001.
- (36) Hlína J, Šonský J, Něnička V, Zachar A. Statistics of turbulent structures in a thermal plasma jet. *Journal of Physics D: Applied Physics* 2005; **38**:1760–1768.
- (37) Hlína J, Gruber J, Šonský J. Application of a CCD camera to investigations of oscillations in a thermal plasma jet. *Measurement Science and Technology* 2006; **17**:918–922.
- (38) Hlína J, Chvála F, Šonský J, Gruber J. Multi-directional optical diagnostics of thermal plasma jets. *Measurement Science and Technology* 2008; **19**:015407.
- (39) Hlína J, Šonský J. Time-resolved tomographic measurements of temperatures in a thermal plasma jet. *Journal of Physics D: Applied Physics* 2010; **43**:055202.

- (40) Viilu A. An experimental determination of the minimum Reynolds number for instability in a free jet. *Journal of Applied Mechanics* 1962; **29**:506–508.
- (41) Dorier J-L, Gindrat M, Hollenstein C, Salito A, Loch M, Barbezat G. Time-resolved imaging of anodic arc root behavior during fluctuations of a DC plasma spraying torch. *IEEE Transactions on Plasma Science* 2001; **29**:494–501.
- (42) Duan Z, Heberlein J. Arc instabilities in a plasma spray torch. *Journal of Thermal Spray Technology* 2002; **11**:44–51.
- (43) Ghorui S, Tiwari N, Meher KC, Jan A, Bhat A, Sahasrabudhe SN. Direct probing of anode arc root dynamics and voltage instability in a dc non-transferred arc plasma jet. *Plasma Sources Science and Technology* 2015; **24**:065003.
- (44) Guisbiers G, Kazan M, Overschelde OV, Wautelet M, Pereira S. Mechanical and thermal properties of metallic and semiconductive nanostructures. *Journal of Physical Chemistry C* 2008; **112**:4097–4103.
- (45) Nemchinsky VA, Shigeta M. Simple equations to describe aerosol growth. *Modelling and Simulation in Materials Science and Engineering* 2012; **20**:045017.
- (46) Girshick SL, Chiu C-P, McMurphy PH. Time-dependent aerosol models and homogeneous nucleation rates. *Aerosol Science and Technology* 1990; **13**:465–477.
- (47) Phanse GM, Pratsinis SE. Theory for aerosol generation in laminar flow condensers. *Aerosol Science and Technology* 1989; **11**:100–119.
- (48) Murphy AB. A comparison of treatments of diffusion in thermal plasmas. *Journal of Physics D: Applied Physics* 1996; **29**:1922–1932.
- (49) Talbot L, Cheng RK, Schefer RW, Willis DR. Thermophoresis of particles in a heated boundary layer. *Journal of Fluid Mechanics* 1980; **101**:737–758.
- (50) Launder BE, Spalding DB. The numerical computation of turbulent flows. *Computer Methods in Applied Mechanics and Engineering* 1974; **3**:269–289.
- (51) McKelliget J, Szekely J, Vardelle M, Fauchais P. Temperature and velocity fields in a gas stream exiting a plasma torch. A mathematical model and its experimental verification. *Plasma Chemistry and Plasma Processing* 1982; **2**:317–332.
- (52) Lee YC, Pfender E. Particle dynamics and particle heat and mass transfer in thermal plasmas. Part III. Thermal plasma jet reactors and multiparticle injection. *Plasma Chemistry and Plasma Processing* 1987; **7**:1–27.
- (53) El-Hage M, Mostaghimi J, Boulos MI. A turbulent flow model for the rf inductively coupled plasma. *Journal of Applied Physics* 1989; **65**:4178–4185.
- (54) Ramshaw JD, Chang CH. Computational fluid dynamics modeling of multicomponent thermal plasmas. *Plasma Chemistry and Plasma Processing* 1992; **12**:299–325.
- (55) Ye R, Proulx P, Boulos MI. Particle turbulent dispersion and loading effects in an inductively coupled radio frequency plasma. *Journal of Physics D: Applied Physics* 2000; **33**:2154–2162.
- (56) Shigeta M, Sato T, Nishiyama H. Numerical simulation of a potassium-seeded turbulent RF inductively coupled plasma with particles. *Thin Solid Films* 2003; **435**:5–12.
- (57) Ahmed I, Bergman TL. Three-dimensional simulation of thermal plasma spraying of partially molten ceramic agglomerates. *Journal of Thermal Spray Technology* 2000; **9**:215–224.
- (58) Hur M, Hong SH. Comparative analysis of turbulent effects on thermal plasma characteristics inside the plasma torches with rod- and well-type cathodes. *Journal of Physics D: Applied Physics* 2002; **35**:1946–1954.
- (59) Ramachandran K, Nishiyama H. Three-dimensional effects of carrier gas and particle injections on the thermo-fluid fields of plasma jets. *Journal of Physics D: Applied Physics* 2002; **35**:307–317.
- (60) Ramachandran K, Kikukawa N, Nishiyama H. 3D modeling of plasma–particle interactions in a plasma jet under dense loading conditions. *Thin Solid Films* 2003; **435**:298–306.
- (61) Ramachandran K, Nishiyama H. Fully coupled 3D modeling of plasma–particle interactions in a plasma jet. *Thin Solid Films* 2004; **457**:158–167.
- (62) Li H-P, Chen X. Three-dimensional modelling of a dc non-transferred arc plasma torch. *Journal of Physics D: Applied Physics* 2001; **34**:L99–L102.
- (63) Li H-P, Pfender E, Chen X. Application of Steenbeck’s minimum principle for three-dimensional modelling of DC arc. *Journal of Physics D: Applied Physics* 2003; **36**:1084–1096.
- (64) Guo Z, Yin S, Liao H, Gu S. Three-dimensional simulation of an argon–hydrogen DC non-transferred arc plasma torch. *International Journal of Heat and Mass Transfer* 2015; **80**:644–652.
- (65) Park JM, Kim KS, Hwang TH, Hong SH. Three-dimensional modeling of arc root rotation by external magnetic field in nontransferred thermal plasma torches. *IEEE Transactions on Plasma Science* 2004; **32**:479–487.
- (66) Mariaux G, Vardelle A. 3-D time-dependent modelling of the plasma spray process. Part 1: Flow modelling. *International Journal of Thermal Sciences* 2005; **44**:357–366.
- (67) Kim KS, Park JM, Choi S, Kim J, Hong SH. Comparative study of two- and three-dimensional modeling on arc discharge phenomena inside a thermal plasma torch with hollow electrodes. *Physics of Plasmas* 2008; **15**:023501 (13 pages).
- (68) Martinez B, Mariaux G, Vardelle A, Barykin G, Parco M. Numerical investigation of a hybrid HVOF-plasma spraying process. *Journal of Thermal Spray Technology* 2009; **18**:909–920.
- (69) Yakhot V, Orszag SA, Thangam S, Gatski TB, Speziale CG. Development of turbulence models for shear flows by a double expansion technique. *Physics of Fluids A* 1992; **4**:1510–1520.
- (70) Colombo V, Concetti A, Ghedini E. Three-dimensional time-dependent modeling of a DC transferred arc twin-torch system. *IEEE Transactions on Plasma Science* 2008; **36**:1038–1039.
- (71) Launder BE, Reece GJ, Rodi W. Progress in the development of a Reynolds-stress turbulence closure. *Journal of Fluid Mechanics* 1975; **68**:537–566.
- (72) Colombo V, Ghedini E. Time dependent 3-D simulation of a non-transferred arc plasma torch: anode attachment and downstream region effects. *Proceedings of 17th International Symposium on Plasma Chemistry*, unpaginated CD, Toronto, Canada, 2005.
- (73) Colombo V, Concetti A, Ghedini E. Time dependent 3D large eddy simulation of a DC non-transferred arc plasma spraying torch with particle injections. *Proceedings of 16th IEEE International Pulsed Power Conference*, Vol. 2, pp. 1565–1568, Albuquerque, USA, 2007.
- (74) Marchand C, Chazelas C, Mariaux G, Vardelle A. Liquid precursor plasma spraying: Modeling the interactions between the transient plasma jet and the droplets. *Journal of Thermal Spray Technology* 2007; **16**:705–712.
- (75) Vardelle A, Chazelas C, Marchand C, Mariaux G. Modeling time-dependent phenomena in plasma spraying of liquid precursors. *Pure and Applied Chemistry* 2008; **80**:1981–1991.
- (76) Colombo V, Concetti A, Ghedini E, Gherardi M, Sanibondi P. Three-dimensional time-dependent large Eddy simulation of turbulent flows in an inductively coupled thermal plasma torch with a reaction chamber. *IEEE Transactions on Plasma Science* 2011; **39**:2894–2895.
- (77) Jeništa J, Takana H, Nishiyama H, Bartlová M, Aubrecht V, Křenek P, Hrabovský M, Kavka T, Sember V, Mašláni A. Integrated parametric study of a hybrid-stabilized argon–water arc under subsonic, transonic and supersonic plasma flow regimes. *Journal of Physics D: Applied Physics* 2011; **44**:435204 (20 pages).
- (78) Shigeta M. Time-dependent 3-D simulation of an argon RF inductively coupled thermal plasma. *Plasma Sources Science and Technology* 2012; **21**:055029.
- (79) Shigeta M. Three-dimensional flow dynamics of an argon RF plasma with dc jet assistance: a numerical study. *Journal of Physics D: Applied Physics* 2013; **46**:015401.
- (80) Trelles JP. Identification of coherent flow structures in non-equilibrium plasmas. *IEEE Transactions on Plasma Science* 2014; **42**:2852–2853.
- (81) Trelles JP, Modirkhazeni SM. Variational multiscale method for nonequilibrium plasma flows. *Computer Methods in Applied Mechanics and Engineering* 2014; **282**:87–131.
- (82) Meillot E, Vincent S, Bot CL, Sarret F, Caltagirone JP, Bianchi L. Numerical simulation of unsteady ArH2 plasma spray impact

- on a moving substrate. *Surface and Coatings Technology* 2015; **268**:257–265.
- (83) Smagorinsky J. General circulation experiments with the primitive equations: I. the basic experiment. *Monthly Weather Review* 1963; **91**:99–164.
- (84) Yoshizawa A. Statistical theory for compressible turbulent shear flows, with the application to subgrid modeling. *Physics of Fluids A* 1986; **29**:2152–2164.
- (85) Kays WM, Crawford ME. *Convective Heat and Mass Transfer*. 3rd ed. McGraw-Hill: New York; 1993.
- (86) Tominaga Y, Stathopoulos T. Turbulent Schmidt numbers for CFD analysis with various types of flowfield. *Atmospheric Environment* 2007; **41**:8091–8099.
- (87) Germano M, Piomelli U, Moin P, Cabot WH. A dynamic subgrid-scale eddy viscosity model. *Physics of Fluids A* 1991; **3**:1760–1765.
- (88) Lilly DK. A proposed modification of the Germano subgrid-scale closure method. *Physics of Fluids A* 1992; **4**:633–635.
- (89) Martín MP, Piomelli U, Candler GV. Subgrid-scale models for compressible large-Eddy simulations. *Theoretical and Computational Fluid Dynamics* 2000; **13**:361–376.
- (90) Kobayashi H. The subgrid-scale models based on coherent structures for rotating homogeneous turbulence and turbulent channel flow. *Physics of Fluids* 2005; **17**:045104.
- (91) Kobayashi H. Large eddy simulation of magnetohydrodynamic turbulent channel flows with local subgrid-scale model based on coherent structures. *Physics of Fluids* 2006; **18**:045107.
- (92) Patanker SV, Spalding DB. A calculation procedure for heat, mass and momentum transfer in three-dimensional parabolic flows. *International Journal of Heat and Mass Transfer* 1972; **15**:1787–1806.
- (93) Oliveira PJ, Issa RI. An improved PISO algorithm for the computation of buoyancy-driven flows. *Numerical Heat Transfer Fundamentals* 2001; **40**:473–493.
- (94) Komurasaki S. A hydrothermal convective flow at extremely high temperature. *Proceedings of 7th International Conference on Computational Fluid Dynamics*, ICCFD7–3001, Kohala Coast, USA, 2012.
- (95) Press WH, Teukolsky SA, Vetterling WT, Flannery BP. *Numerical Recipes in C the Art of Scientific Computing*. 2nd ed. Cambridge University Press: Cambridge; 1992.
- (96) Watanabe T, Honda T, Kanzawa A. Concentration of a plasma energy flow by a blowing gas. *International Chemical Engineering* 1989; **29**:663–670.
- (97) Matsushita Y. Outflow boundary condition in the finite volume method for unsteady-state fluid flow computation with variable density. *Computational Thermal Sciences* 2011; **3**:531–537.
- (98) Menart J, Lin L. Numerical study of high-intensity free-burning arc. *Journal of Thermophysics and Heat Transfer* 1998; **12**:500–506.
- (99) Japan Institute of Metals. *Metal Data Book*. Maruzen: Tokyo; 1993 in Japanese.
- (100) Leparoux M, Schreuders C, Shin JW, Siegman S. Induction plasma synthesis of carbide nano-powders. *Advanced Engineering Materials* 2005; **7**:349–353.
- (101) Rao N, Girshick SL, Heberlein J, McMurtry P, Jones S, Hansen D, Micheel B. Nanoparticle formation using a plasma expansion process. *Plasma Chemistry and Plasma Processing* 1995; **15**:581–606.
- (102) Leparoux M, Kihn Y, Paris S, Schreuders C. Microstructure analysis of RF plasma synthesized TiCN nanopowders. *International Journal of Refractory Metals and Hard Materials* 2008; **26**:277–285.
- (103) Leparoux M, Schreuders C, Fauchais P. Improved plasma synthesis of Si-nanopowders by quenching. *Advanced Engineering Materials* 2008; **10**:1147–1150.
- (104) Berlinger B, Benker N, Weinbruch S, L’Vov M, Ebert W, Koch DGE, Thomassen Y. Physicochemical characterisation of different welding aerosols. *Analytical and Bioanalytical Chemistry* 2011; **399**:1773–1780.

Masaya Shigeta (Non-member) received the Ph.D. degree from the Graduate School of Engineering, Tohoku University (TU), in 2004. He worked as a Post-Doctoral Research Fellow at the Tokyo Institute of Technology in 2004 and at the University of Minnesota (USA) in 2005. He was an Assistant Professor with TU during 2006–2013. Since 2013, he has been an Associate Professor at the Joining and Welding Research Institute, Osaka University. He was also a Visiting Professor at the University of Bologna (Italy) in 2010 and a Visiting Scholar at the University of California, Berkeley (USA) in 2012, concurrently. Dr. Shigeta received the Young Scientists’ Prize, the Commendation for Science and Technology by the Minister of Education, Culture, Sports, Science and Technology of Japan, in 2014. He was invited to present his work at the highly recognized international conference “Gordon Research Conference on Plasma Processing Science” in 2014. He has concurrently been a delegated member of the Japan Society of Fluid Mechanics, a committee member on Public Information of Fluid Engineering Division in the Japan Society of Mechanical Engineers, a reviewing committee member of the Japan Welding Society, an editorial board member of the Smart Processing Society for Materials, and an auditor of KANSAI branch of the Japan Welding Society. Furthermore, he has concurrently been a member of the External Advisory Board on the European Union’s Horizon 2020 Research and Innovation Programme since 2015.

